International Journal of Microwave and Wireless Technologies

cambridge.org/mrf

Highly miniaturized wideband angular stable linear–circular and linear–cross polarization converter for Ka-band satellite applications

Mohammad Abdul Shukoor and Sukomal Dey

Department of Electrical Engineering, Indian Institute of Technology Palakkad, Palakkad, Kerala 678557, India

Research Paper

Cite this article: Shukoor MA, Dey S (2023). Highly miniaturized wideband angular stable linear–circular and linear–cross polarization converter for Ka-band satellite applications. *International Journal of Microwave and Wireless Technologies* **15**, 1557–1569. https://doi.org/10.1017/S1759078723000417

Received: 27 January 2023
Revised: 24 March 2023
Accepted: 27 March 2023

Keywords:
Angular stable; compact; linear–circular; linear–cross; miniaturized; polarization converter; wideband

Corresponding author:
Sukomal Dey;
Email: sukomal.iitpkd@gmail.com

Abstract

This work proposes a novel, extremely miniaturized wideband linear–circular and linear–cross metasurface-enabled reflective polarizer. This design comprises a Meander-line structure with horizontal dipoles as the top frequency selective surface, printed on a 1 mm thin-grounded FR-4 substrate. The *x*/*y*-polarized incident electromagnetic wave is converted as circularly polarized from 10.60 to 10.92 GHz (LHCP/RHCP), 12.12 to 17.32 GHz (RHCP/LHCP), and 22.72 to 37.76 GHz (LHCP/RHCP) during reflection with 2.97, 35.33, and 49.74% Fractional Bandwidth (FBW). In addition, this design shows linear–cross conversion with a minimum 90% polarization conversion ratio from 11.41 to 12, 19.01 to 22.34, and 40.74 to 46.82 GHz with an FBW of 5.04, 16.11, and 13.89%. The device performance is considerably stable under different oblique incidences, and the polarizer's unitcell is compact with a structural periodicity of $0.089 \times 0.064\ \lambda_L^2$, and ultra-thin low-profile substrate thickness of $0.035\lambda_L$. The proposed prototype is fabricated, and the measured results are in good agreement with the simulated one. This article also mentions how this polarizer could be tuned for dual-band K- and Ka-band satellite applications. The authors believe that the design's novelty lies in the multiband conversion with circular-polarization orthogonality, a highly miniaturized unitcell's volume of $0.199\ \lambda_L^3/1000$, and better angular stability made this design a potential candidate for real-time satellite applications.

Introduction

Wave polarization is an essential feature, regulating the polarization state of the electromagnetic (EM) wave is used in various applications such as polarization manipulation [1], wavefront controlling [2], and optical communication [3]. birefringent-based wave plates, crystalline solids, and liquids modify EM wave polarization [4]. In order to accommodate the hundreds of times greater thickness required by the weak anisotropic natural crystals, these converters are incredibly bulky and consumes more power. The ever-more miniaturized systems necessitate the development of low-profile devices [5].

The development of frequency selective surface (FSS) technology [6, 7] has boosted the researcher's community in the design of different two-dimensional polarizers for advanced wireless applications [8]. Note that circular polarization (CP) is impervious to the effects like Faraday rotation, multipath fading, and polarization mismatch compared to linear polarization [9]. But the inherent drawbacks of circularly polarized antennas like narrow bandwidth, complex feeding, and polarization orthogonality made FSS-based linear-to-circular polarization converters (LCPCs) compulsory candidates to exploit all features like wideband and so on, which are lacking and difficult to implement with direct CP antennas [10].

An H-shaped dipole-based linear–cross and circular–circular reflective polarizer is exhibited for K-and Ka-band applications [11]. Since the circularly polarized wave's rotation sense changes after encountering any barrier, maintaining the wave handiness is also critical in many applications. Michele *et al.* proposed the optimal design of miniaturized wideband angular stable polarization conversion using the genetic algorithm approach [12]. Zhao *et al.* proposed a compact and high efficient linear–cross miniaturized w-shaped asymmetric FSS with a polarization conversion ratio (PCR) above 90% from 8.44 to 24.96 GHz [13]. The concentric rectangular pattern-based metasurface is presented to regulate linear and circularly polarized waves in dual bands from 4.40 to 5.30 GHz and 9.45 to 13.60 GHz [14]. Two linear–circular polarizers were presented, i.e. one operating from 6 to 6.5 GHz, and the second being operating in the dual band from 4.58 to 5.13 and 6.0 to 6.4 GHz with bandwidths of 550 and 400 MHz, respectively [15]. The proposed research provides a new rationale for favoring the meta-concrete definition with potential future radome designs. The research on metasurface will focus on developing new fiber-based microwave shielding and cloaking technologies. A broadband ultrathin ($\sim\lambda/70$) linear–circular polarizer with an invertibility feature is demonstrated in [16]. The induced anisotropic optical resonances made this single-layered substrate

design able to convert linearly polarized waves into circular ones and the other way around. In addition, broadband LCPCs are implemented in two different modes using solid-state plasma metasurface with a minimum 3 dB axial ratio (AR) bandwidth ranging from 14.34 to 19.61 GHz (mode-1) and 8.81 to 14.34 GHz (mode-2) [17]. The transmission line equivalent circuit approach is detailed for designing dual-band CP converters [18]. Lin *et al.* proposed an ultra-wideband LCPC with 112% fractional bandwidth (FBW) (5.8–20.4 GHz) utilizing a corner-truncated circular patch [19]. A reflective polarizer that can convert linearly polarized wave into its orthogonal in the lower band (6.53–12.07 GHz) and circularly polarized in the upper band (13.70–15.60 GHz) is presented in [20]. This simple design comprises a 45° tilted dipole separated by two meander-line-like structures. Also, flexible substrate-based linear–cross reflective polarizers for conformal application exhibit an average of 85% PCR in X and Ku-bands [21]. Various polarizers like metallic three-dimensional FSS-based [22] were also introduced, from microwave [23] to optical regimes [24], which are reported in the literature.

In Satcom applications, along with the CP, it is preferred that antennas are required to operate at two distinct, non-adjacent frequency bands in orthogonal polarizations to further enhance the isolation between transmitted and received signals [9]. Due to extremely low power flux densities, the system environment is highly susceptible to interference in real time [8]. Dual-band, dual-CP patch antennas can be used as the terminal antenna in a phased array [25]. However, at Ka-band frequencies, these solutions are either cumbersome and expensive or tiny but inefficient and difficult to make. There is a need for low-profile, low-cost, and easily fabricated devices in the millimeter-wave frequency range and beyond. LCPCs mounted with antennas were used to overcome the above-mentioned limitations [26]. In addition, the polarizer metasurface should perform at greater oblique angles since there is no guarantee that the incident wave will always be in the normal direction in real time. As a result, destructive interference occurs at increasingly larger oblique angles and higher frequency ranges due to the increased path taken by the EM wave within a dielectric spacer [11].

By considering all these, a simple reflective polarizer is proposed in this work which performs LCPC in three different bands with a bandwidth of 0.32 GHz (LHCP/RHCP in X-band), 5.2 GHz (RHCP/LHCP in Ku), and 15.04 GHz (LHCP/RHCP in K- and Ka-bands). In addition, it can also perform linear–cross polarization conversion having bandwidths like 0.59 GHz (X-band), 3.33 GHz (K-band), and 6.08 GHz (V-band). The design is highly compacted (unitcell area of 0.569 $\lambda_L^2/100$) with considerable angular stability up to 45° for transverse electric (TE) and transverse magnetic (TM) modes along with the CP orthogonality.

Conversely, a dedicated frequency spectrum is used in Ka-band for downlink (D/L) at 17.7–20.2 GHz and uplink (U/L) at 27–30 GHz for high-speed satellite communications. After receiving a left-handed CP field, the user's ground terminal should broadcast an orthogonal right-handed CP (RHCP) field back to the sender opposite to the received D/L signal. For this purpose, the proposed design's central portion is connected with a metallic strip of a particular width such that the orthogonal LCPC bands shift to 17.73–19.35 GHz (LHCP/RHCP) and 27.02–36.20 GHz (RHCP/LHCP). This design shows its capability to work for dedicated Satcom application frequencies and other bands where the linear–circular (with orthogonality) and linear–cross conversion is the primary concern.

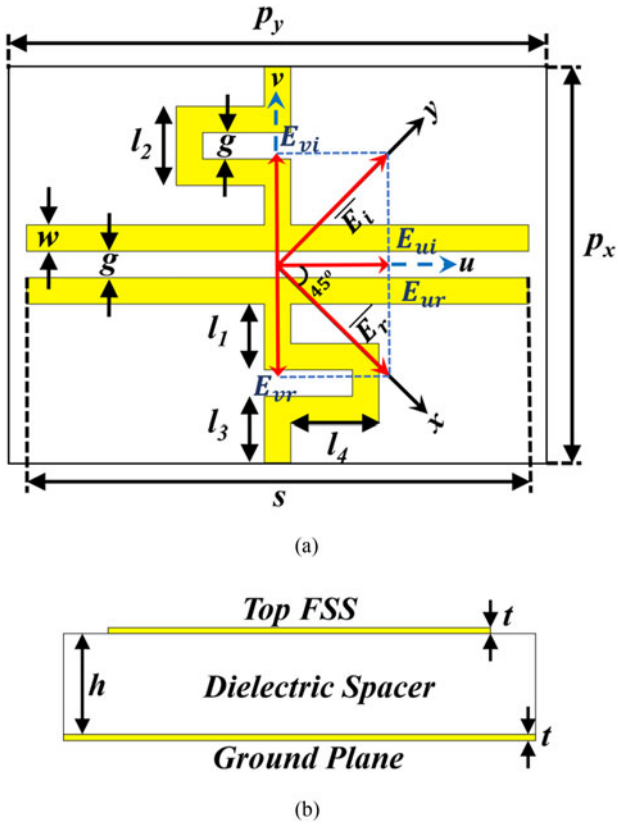

Fig. 1. (a) Top view and (b) side view of the proposed reflective polarizer.

The paper is organized as follows. The design of the unitcell and simulation results are discussed in Section "Unitcell design and the simulation results." A transfer matrix method (TMM) is employed for analysis, and the extracted equivalent circuit is discussed in Section "Analysis and discussion." The design can be transformed to work for K- and Ka-band real-time satellite communication frequencies. The device is fabricated, and the obtained result is compared with the simulated one in Section "Prototype fabrication and measured results." The proposed design performance is compared with the other state-of-the-art designs reported in the literature in Table 3, and finally, the conclusion is drawn in the final section.

Unitcell design and the simulation results

The unitcell of the multiband linear–circular and linear–cross reflective type polarizer is shown in Fig. 1. The top FSS and ground plane are sandwiched on either side of a dielectric spacer. The top FSS constitutes a meander-line-based inductor separated by orthogonal dipoles that generate the capacitance effect. The commercially available FR-4 substrate (relative permittivity ε_r = 4.4, and loss-tangent tan δ = 0.02) is used as a dielectric spacer, and a 0.035 mm (=t) thin copper film with conductivity σ = 5.8×10^7 S/m is utilized as the metallic layer. Finite-element method-based solver ANSYS HFSS is used to optimize the final unitcell's dimensions for the desired performance by applying appropriate master–slave periodic boundary conditions, mimicking the infinite array. The final unitcell dimensions are: p_x = 1.8 mm, p_y = 2.52 mm, h = 1 mm, s = 2.28 mm, l_1 = 0.3 mm, l_2 = 0.36 mm, l_3 = 0.3 mm, l_4 = 0.4 mm, w = 0.12 mm, and g = 0.12 mm, as shown in Fig. 1(a). Here, p_x, p_y denote the unitcell periodicity

https://doi.org/10.1017/S1759078723000417 Published online by Cambridge University Press

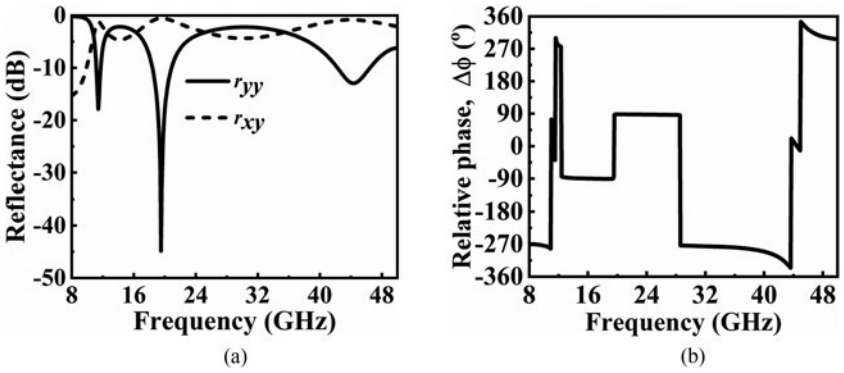

Fig. 2. Simulated (a) magnitudes of r_{yy} and r_{xy}. (b) Relative phase ($\Delta\phi$).

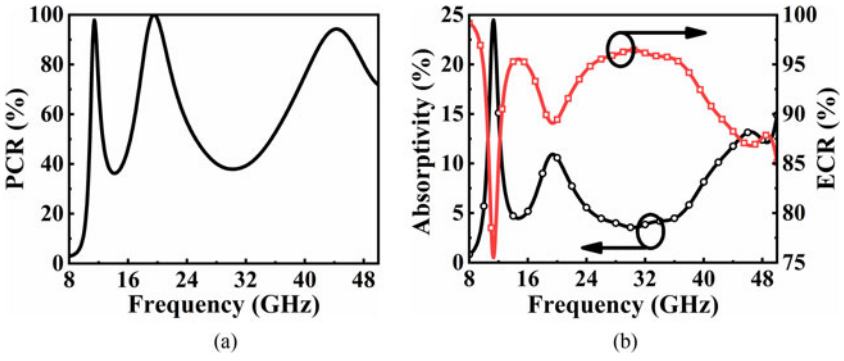

Fig. 3. Simulated (a) PCR. (b) Absorption and ECR of the reflective polarizer.

along the x and y axes, h is the substrate thickness, l_i ($i = 1$–4) are the lengths, w is the line's trace width, and g represents the gap. The reflective type polarization converter is opted for the inherent broadband performance to serve the purpose.

For the y-polarized EM wave incident on the polarizer's metasurface (see Fig. 1), the co-pol $r_{yy} = |E_{yr}|/|E_{yi}|$, and the cross-pol $r_{xy} = |E_{xr}|/|E_{yi}|$ reflectances are defined. The terms E_i, and E_r refer to the incident and reflected electrical field components, and the indices x, and y represent field oscillating directions.

The simulated reflectances of the polarizer for the y-polarized incidence are shown in Fig. 2. The response in Fig. 2(a) depicts that co-pol reflectance approaches minimum, i.e. −17.88, −39.93, and −12.94 dB at three different resonant frequencies, 11.4, 19.54, and 44.3 GHz. However, the cross-pol reflectance approaches near-unity (≈0 dB), illustrating perfect linear–cross conversion in these three bands. For any reflective polarizer, $PCR = r_{xy}^2/(r_{xy}^2 + r_{yy}^2)$ defines the efficiency of linear–cross conversion, and the simulated PCR of the proposed design is shown in Fig. 3(a). It shows PCR of above 90% from 11.41–12 GHz (X-band), 19.01–22.34 GHz (K-band), 40.74–46.82 GHz (V-band) with an FBW of 5.04, 16.11, and 13.89%, respectively.

In the reflective polarizer's design, it is necessary to know the total amount of the incident energy dissipating in the substrate along with its conversion efficiency. The absorptivity, $A(\omega) = 1 - |r_{yy}|^2 - |r_{xy}|^2$, and energy conversion ratio (ECR), $ECR = |r_{yy}|^2 + |r_{xy}|^2$ are calculated, and the results are depicted in Fig. 3(b). Almost 90% of incident energy is transformed into different polarizations, and the remaining portion is accounted for as the dielectric losses over the operating frequency range. In addition to the linear–cross conversion, the design also demonstrates linear–circular conversion characteristics at other frequency bands. From Fig. 2, the magnitudes of the co- and cross-pol reflectances are almost equal (crossing each other around 3 dB) in three frequency bands (see Fig. 2(a)). The relative phase ($\Delta\phi$) between the co- and cross-pol reflectances is calculated, and it is ±90° in those frequency bands, as shown in Fig. 2(b). Since the CP is the ideal case, the efficiency of the linear–circular conversion is measured by the term AR which has been calculated, as in [20]:

$$R = \frac{r_{xy}}{r_{yy}} \tag{1}$$

$$Schi,\ \chi = 0.5\sin^{-1}\left(\frac{2R\sin(\Delta\phi)}{1+R^2}\right) \tag{2}$$

$$Axial\ Ratio,\ AR = |1/\tan(\chi)| \tag{3}$$

From Fig. 4(a), it is clear that the proposed converter results in the AR ≤ 3 dB response from 10.60 to 10.92 GHz (X-band), 12.12 to 17.32 GHz (Ku-band), and 22.72 to 37.76 GHz (Ka-band) with 2.97, 35.33, and 49.74% FBW, respectively. In order to detrmine the CP handedbness, the expression for the ellipticity (e) is given below:

$$\text{Ellipticity},\ e = \frac{2|r_{xy}||r_{yy}|\sin(\Delta\phi)}{|r_{xy}|^2 + |r_{yy}|^2} \tag{4}$$

The ellipticity ranges from −1 (RHCP) to +1 (LHCP). Different circular senses of rotation in the consecutive bands are observed from simulated ellipticity, as shown in Fig. 4(b). It is noteworthy that the polarizer is dual-polarized. The

https://doi.org/10.1017/S1759078723000417 Published online by Cambridge University Press

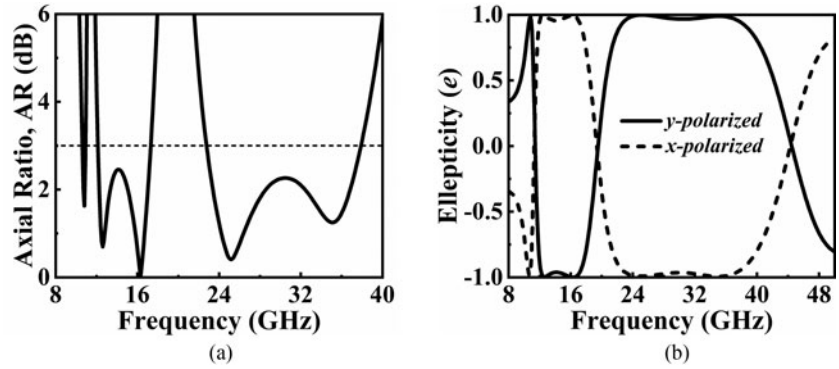

Fig. 4. Simulated (a) AR. (b) Ellipticity (*e*) of the proposed reflective polarizer.

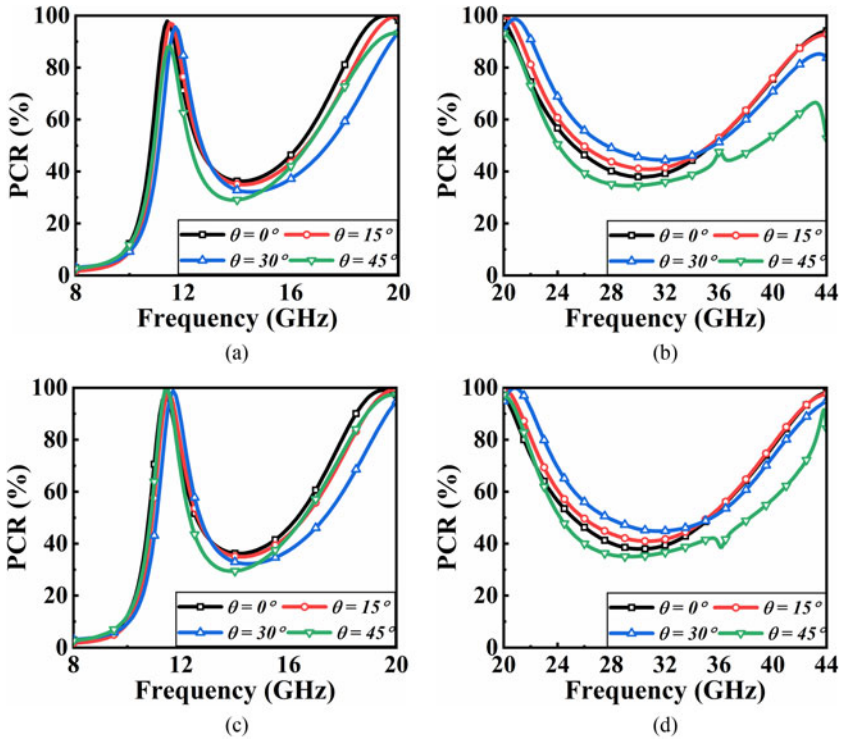

Fig. 5. Simulated PCR for different incident angles under TE for (a) X, Ku, and (b) K, Ka-bands. Under TM incidence of the proposed reflective polarizer for (c) X, Ku, and (d) K, Ka-bands.

handedness of CP interchanges if the *y*-polarized incidence is changed with the *x*-polarized.

Next, the performance of the proposed polarizer is subjected to different incident angles from 0° to 45°, in steps of 15° for both TE and TM cases. The simulated PCR and AR (dB) for TE and TM incidences are shown in Figs 5 and 6, respectively. The PCR computation deals with reflectance magnitudes, but the reflection phases explain its behavior better at higher oblique angles [27]. The PCR bandwidth is reduced when the incidence angle is shifted away from the normal. It is also noticed that the cross-pol (r_{xy}) is nearly unaltered in amplitude and phase, while the co-pol (r_{yy}) reflectance is highly dependent on the incidence angle. As a result, the extra traveling path between the FSS and ground at higher angles results in a more r_{yy} phase. This extra phase would deteriorate the PCR performance. It can be calculated by the Bragg diffraction formula [21] as below:

$$\Delta\phi = \phi_{oblique} - \phi_{normal} = 2\sqrt{\varepsilon_r}kd\left(\frac{1}{\sqrt{1-(\sin^2\theta/\varepsilon_r)}} - 1\right) \quad (5)$$

Here, θ denotes the incident angle concerning normal, d is the substrate thickness, and k is the wave vector within the substrate. From Fig. 5, the PCR response is almost stable up to 45°, but a small disturbance is observed at a higher frequency region for the TM case at higher oblique angles, as in [11], and the reduction in PCR level is due to weak field couplings at higher angles. The AR (dB) is almost stable up to 45° with a slight reduction of AR (≤3 dB) bandwidth in the higher frequency band (see Fig. 6). The detailed working analysis of the reflective polarizer is included in the subsequent section.

Analysis and discussion

Analysis using TMM

Two axes, *u*- and *v*-, are defined at 45° counterclockwise to the *x*–*y* to gain insight into the physical mechanism behind the polarization conversion (see Fig. 1). The incident electric field for the wave propagating along the negative *z*-direction can be written as $\vec{E_i} = (E_i^u\tilde{u} + E_i^v\tilde{v})e^{jkz}$, where E_i^u, and E_i^v are the components

https://doi.org/10.1017/S1759078723000417 Published online by Cambridge University Press

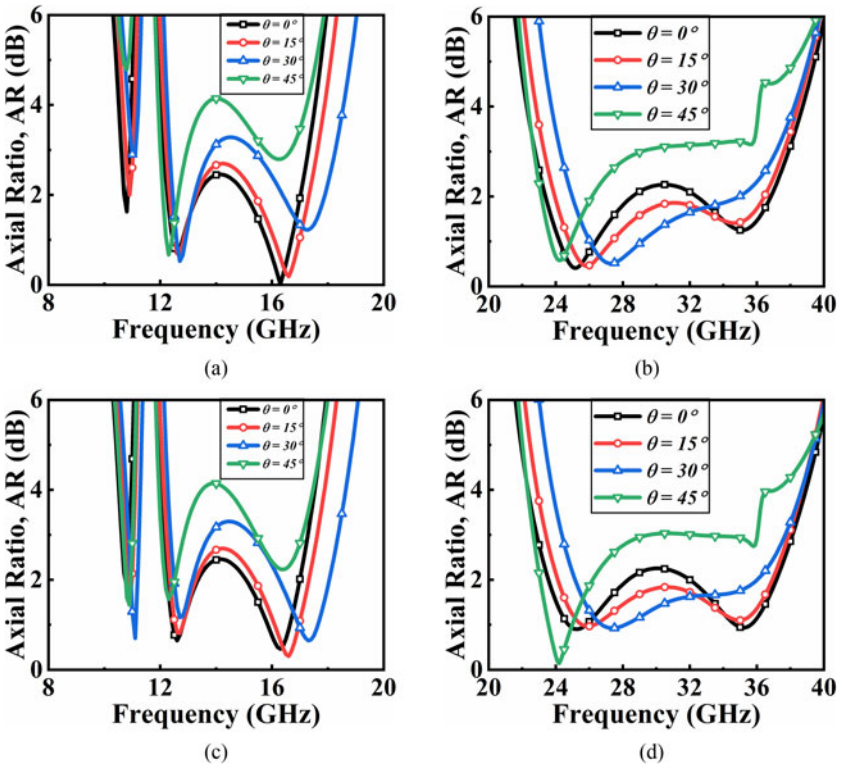

Fig. 6. Simulated AR for different incident angles under TE for (a) X, Ku, and (b) K, Ka-bands. Under TM incidence of the proposed reflective polarizer for (c) X, Ku, and (d) K, Ka-bands.

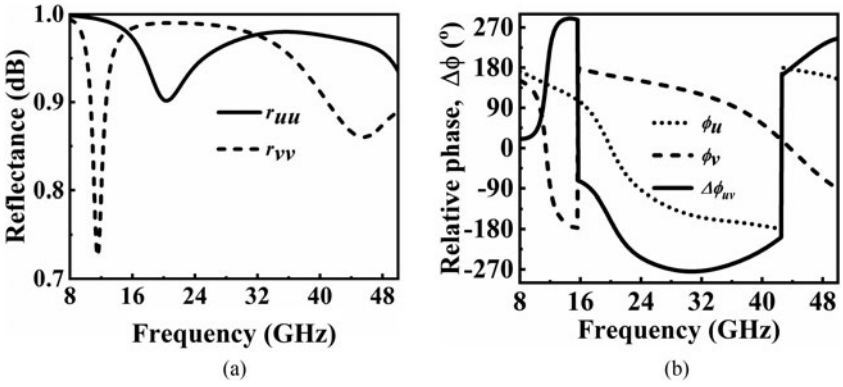

Fig. 7. Simulated (a) magnitudes of r_{uu} and r_{vv}. (b) Relative phase ($\Delta\phi_{uv}$).

along u and v-axes. From the TMM technique, the reflected field components can be written as $[\vec{E_r}] = [R_{lin}][\vec{E_i}]$. Here $[R_{lin}]$ is the reflection matrix as given below:

$$\begin{bmatrix} E_r^u \\ E_r^v \end{bmatrix} = \begin{bmatrix} r_{uu} & r_{uv} \\ r_{vu} & r_{vv} \end{bmatrix} \begin{bmatrix} E_i^u \\ E_i^v \end{bmatrix} \tag{6}$$

Since the unitcell design is symmetric about uv-axes, the effect of the cross-pol reflectance is minimal and can be neglected. Then, the reflected field component can be written as

$$\vec{E_r} = (r_{uu}E_i^u\tilde{u} + r_{vv}E_i^v\tilde{v})e^{-jkz} \tag{7}$$

The simulated magnitudes and phases of the r_{uu} and r_{vv} are shown in Fig. 7. From the response shown in Fig. 7(a), the magnitudes of r_{uu} and r_{vv} are almost unity over the band with a small dip at frequencies 11.5, 20.3, and 45.6 GHz. The eigenmodes at frequencies 11.5 and 45.6 GHz is stronger (higher Q-factor) than the mode at 20.3 GHz. If the loss of substrate is neglected, then $r_{uu} = e^{j\phi_u}$, $r_{vv} = e^{j\phi_v}$, and $\Delta\phi = \phi_u - \phi_v$, where $\Delta\phi$ is the relative phase. The different possible conversions for different magnitudes and phases of r_{uu} and r_{vv} are summarized in Table 1. The equivalent circuit of the polarizer is extracted and is detailed in the next section.

Equivalent circuit modeling of the proposed converter

The polarizer's transmission line equivalent circuit model for a better understanding of the polarization conversion phenomena is extracted for u- and v-polarized incidences (see Fig. 1), as shown in Fig. 8. A similar procedure is used for the extraction, as detailed in [28]. The top FSS is modeled as a combination of series and parallel LC circuit elements. Accordingly, the metallic conductor and dielectric losses are modeled as lumped resistors. The short circuit is taken to mimic the perfect ground (for

https://doi.org/10.1017/S1759078723000417 Published online by Cambridge University Press

Table 1. Summary of polarization conversion for different magnitudes and relative phases

Sl. no.	ϕ_u	ϕ_v	$\Delta\phi = \phi_u - \phi_v$	r_{uu}	r_{vv}	Reflected field ($\vec{E_r}$)	Polarization conversion
1	π	0	$+\pi$	-1	$+1$	$\vec{E_r} = (-E_i^u\tilde{u} + E_i^v\tilde{v})e^{-jkz}$	Linear–cross (negative *x*-direction)
2	0	π	$-\pi$	$+1$	-1	$\vec{E_r} = (+E_i^u\tilde{u} - E_i^v\tilde{v})e^{-jkz}$	Linear–cross (positive *x*-direction)
3	$-\pi/2$	$+\pi$	$+\pi/2$	$-j$	-1	$\vec{E_r} = (-jE_i^u\tilde{u} - E_i^v\tilde{v})e^{-jkz}$	Linear–circular (LHCP)
4	$+\pi/2$	$-\pi$	$-\pi/2$	$+j$	-1	$\vec{E_r} = (+jE_i^u\tilde{u} - E_i^v\tilde{v})e^{-jkz}$	Linear–circular (RHCP)

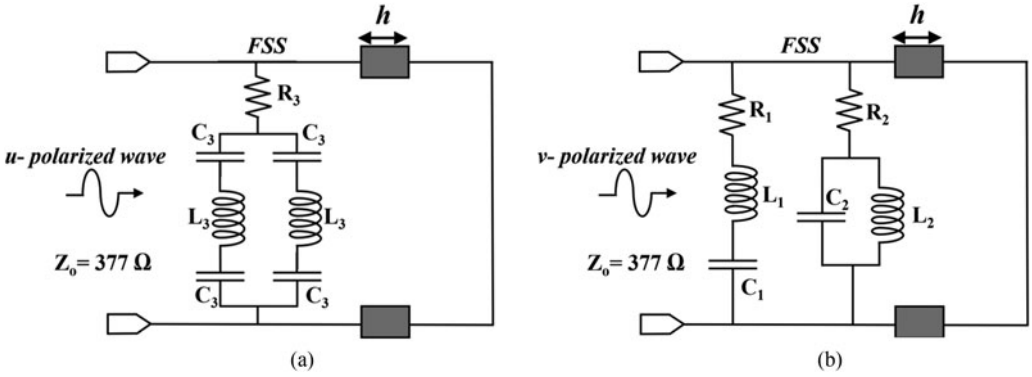

Fig. 8. Equivalent circuit model of the proposed polarizer for (a) *u*- and (b) *v*-polarized incidence.

Table 2. Lumped components values of the equivalent circuit model

R_1	L_1	C_1	R_2	L_2	C_2
3.6	0.75	95	4.7	8	16
R_3		L_3		C_3	
5.21		1.3		29.5	

Note: The units for *R*, *L*, and *C* are in Ω, nH, and fF, respectively.

reflection type). The transmission line of length "*h*" with respective characteristic impedance is chosen for the dielectric substrate. Primarily, the inductances and capacitances values are calculated first from the expressions below [29]:

$$L_i = \frac{\mu_o L}{2\pi}\ln\left(\sin\left(\frac{\pi m}{2L}\right)^{-1}\right) \quad \text{for } i = 1,\ 2,\ 3. \tag{8}$$

$$C_j = \frac{2\varepsilon_o\varepsilon_{eff} L}{\pi}\ln\left(\sin\left(\frac{\pi n}{2L}\right)^{-1}\right) \quad \text{for } j = 1,\ 2,\ 3. \tag{9}$$

Here, the coupling between the orthogonal components is negligible [9]. The top FSS is modeled series RLC for the *u*-polarization excitation. Series and parallel LC circuits were combined for *v*-excitation (see Fig. 8(b)). Here μ_o, ε_o are the permittivity and permeability of the free space (or vacuum). The $\varepsilon_{eff} = \sqrt{(\varepsilon_r + 1)/2}$ is considered as effective permittivity. The terms *m* and *n* are calculated as detailed in [9]. Initially, the calculated values are used in the Keysight ADS circuit simulator, and the curve fitting technique is used to extract the final values of the lumped components, as tabulated in Table 2. The simulated magnitude response of r_{uu} and r_{vv} extracted from the circuit simulator is compared with the EM solver response, and a good agreement is observed, as shown in Fig. 9. The surface currents are field distribution for different resonant frequencies are investigated in the next section.

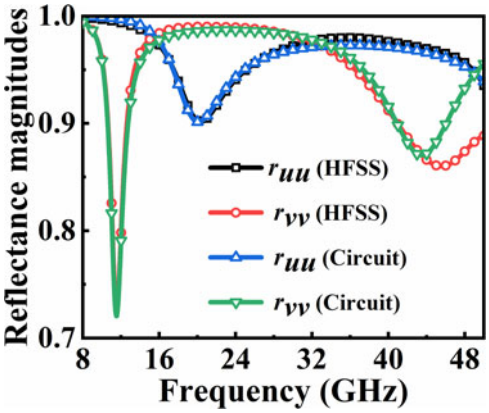

Fig. 9. Reflectances extracted from circuit simulator with EM solver.

Surface current and electric field distribution analysis

In this section, the surface current distribution of the proposed polarizer of the top FSS and ground are analyzed for a better understanding of the physics lying behind the polarization conversion phenomena. When a polarizer excites at 45°, the symmetric and asymmetric coupling of the electric and magnetic fields induces currents in both top polarizer FSS and ground. From Fig. 10, the response induces in the FSS and ground are antiparallel (180° out of phase) for both the resonant frequencies 11.2 and 19.1 GHz, as shown in Fig. 10.

https://doi.org/10.1017/S1759078723000417 Published online by Cambridge University Press

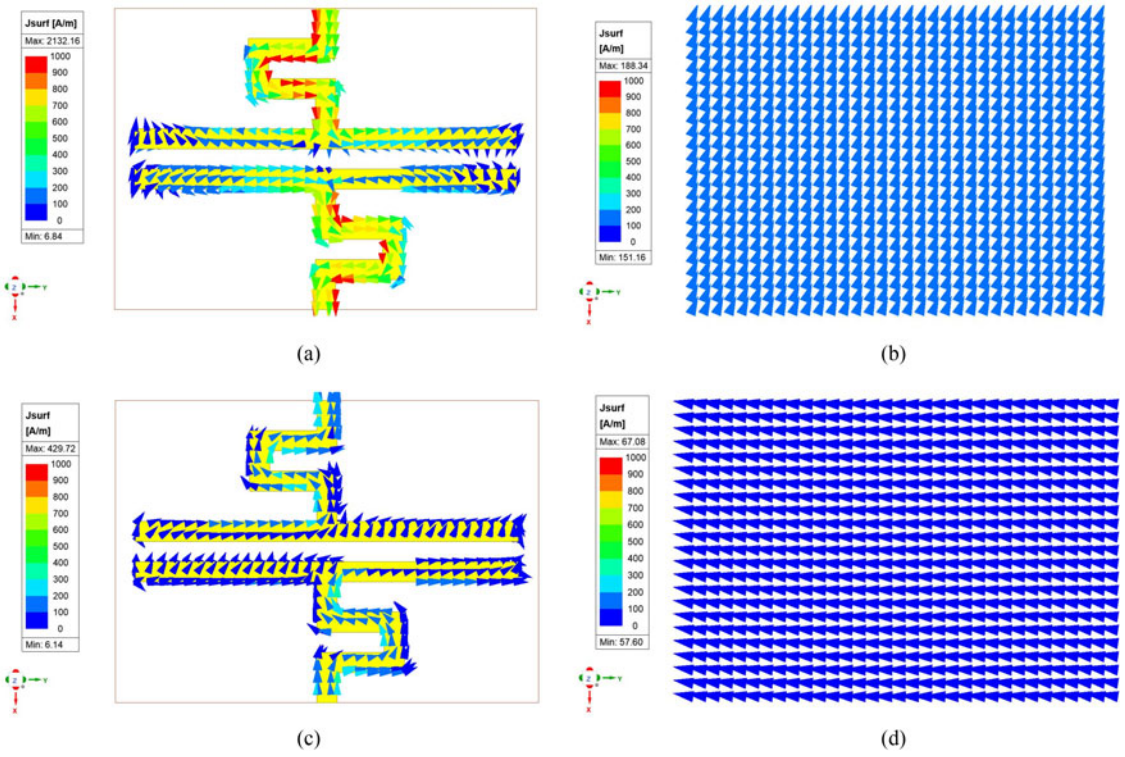

Fig. 10. Simulated surface distributions of the (a) top FSS, (b) ground at 11.2 GHz, and for the (c) top FSS, (d) ground at 19.1 GHz.

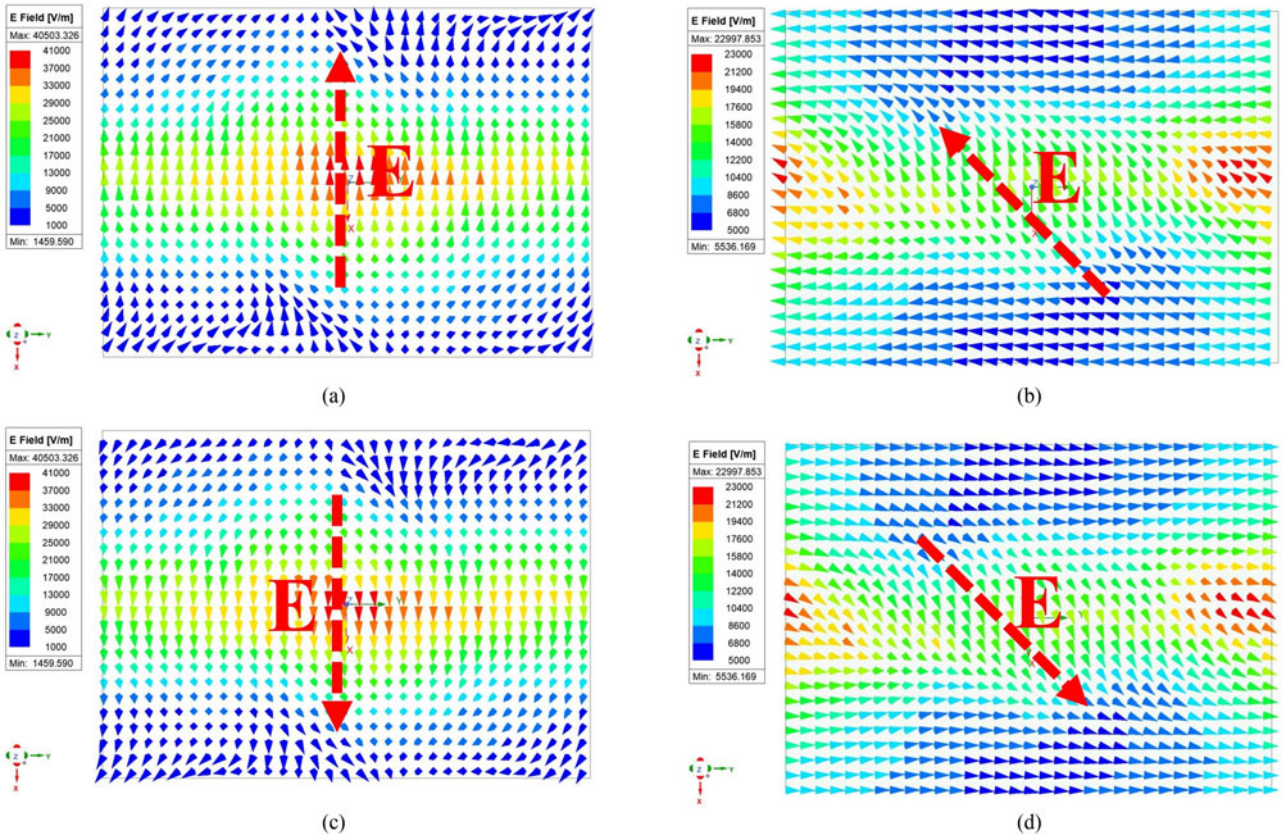

Fig. 11. Simulated electric field patterns at the incident phase: (a) 0°, (b) 90°, (c) 180°, and (d) 270° for 12.6 GHz.

https://doi.org/10.1017/S1759078723000417 Published online by Cambridge University Press

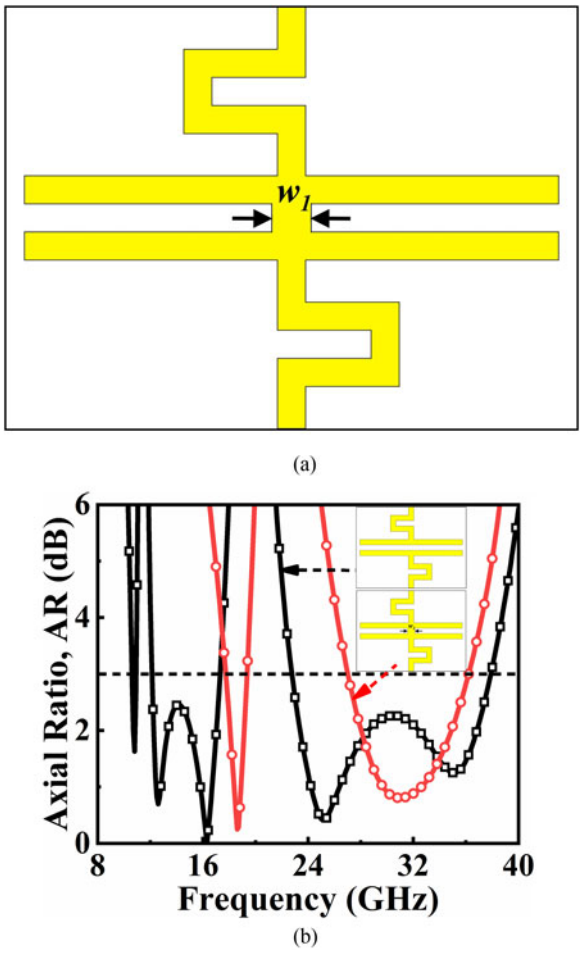

Fig. 12. Comparison of the AR variation for different configurations of the proposed cell.

Since the design performs linear–circular conversion along with linear–cross, the electric field distribution profiles have been investigated at 12.6 GHz at different incident phases, as shown in Fig. 11. A plane has been assigned near the proposed polarizer FSS. The simulated electric field pattern depicts that the design converts the *y*-polarized linear incidence to the RHCP wave. Similar analysis can be carried out for different frequencies to verify the handedness of CP. Next, the proposed design analysis for the transformation to work for the satellite application frequencies is presented.

Transforming the proposed polarizer for K- and Ka-band satellite communication

In the future of wireless applications, satellite communications will be increasingly significant. A dual-band dual-polarization in adjacent mode CP antenna is required for K/Ka-band satellite communications. As a result, it should be capable of operating from 17.7 to 20.2 and 27 to 30 GHz simultaneously with an improved polarization mismatch ratio [26]. The highly miniaturized multiband linear–circular with CP orthogonality in the consecutive bands reflective polarizer is demonstrated in the proposed work (see Fig. 1). This design shows linear–circular polarization in operational bands, i.e. 10.60–10.92, 12.12–17.32, and 22.72–37.76 GHz. But the design is easily configurable to resonate in the Satcom application frequencies by simply connecting the two dipoles with the metallic strip of width w_1, as shown in Fig. 12(a). The value of w_1 was found to be 0.14 mm by parametric optimization. The simulated AR of the modified cell is compared with the earlier response without a metallic strip connected between the two dipoles, as shown in Fig. 12(b). It shows 3 dB AR in the frequency range from 17.73 to 19.35 and 27.02 to 36.20 GHz covering the K- and Ka-bands of the satellite applications.

Prototype fabrication and measured results

For the validation of the simulated results, the prototype of a 30×40 array (75.6×72 mm^2) is fabricated using conventional printed circuit board technology (see Fig. 13(a)). The free-space measurement method is adopted to extract the fabricated sample's reflectances [27], as depicted in Fig. 13(b). This setup consists of two high-gain horn antennas (transmitting and receiving), connected to the Keysight Power Network Analyzer (PNA) N5224B through high-end RF connecting probes operating from 10 MHz to 43.5 GHz. The sample is placed in the far-field zone of the horn antennas and is aligned at 45° (see Fig. 13(b)), at a distance of 30 cm from the antennas. These antennas were separated by 5° to ensure maximum power incidence from the transmitter and reflected to the receiver under normal incidence. The PNA calibration is done by a perfect electric conductor having similar dimensions

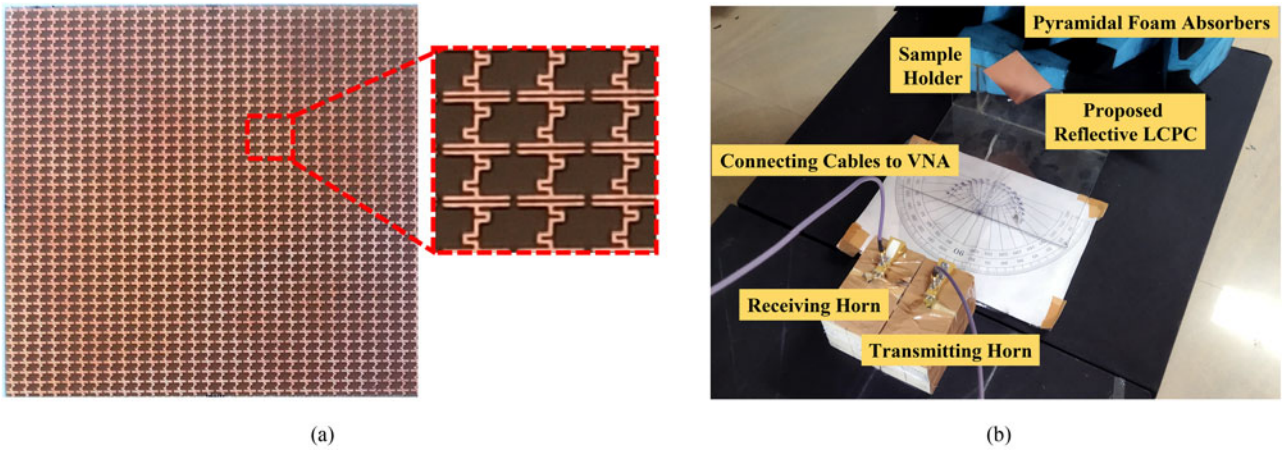

Fig. 13. (a) The top-view of the fabricated prototype. (b) Free-space measurement experimental setup.

https://doi.org/10.1017/S1759078723000417 Published online by Cambridge University Press

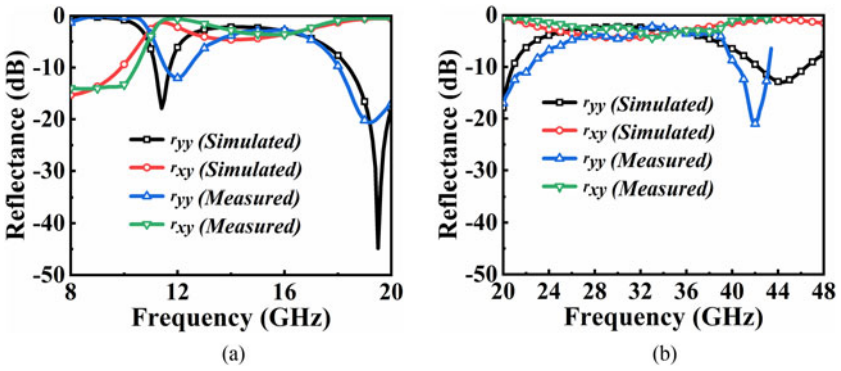

Fig. 14. Comparison of simulated versus measured reflectances (r_{yy} and r_{xy}) for (a) X, Ku, and (b) K, Ka-bands.

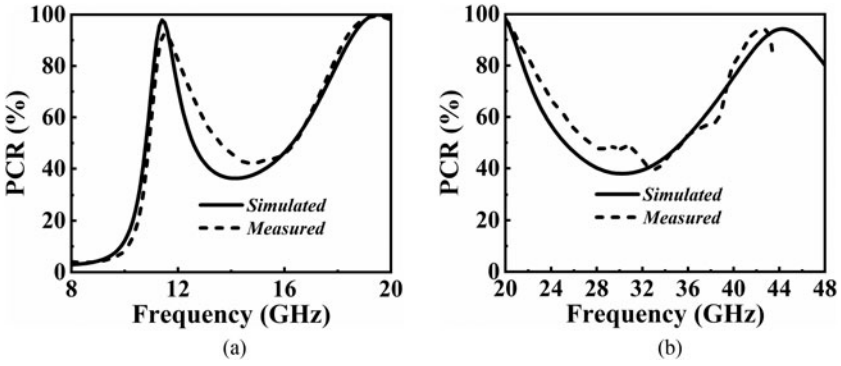

Fig. 15. Comparison of simulated versus measured PCR for (a) X, Ku, and (b) K, Ka-bands.

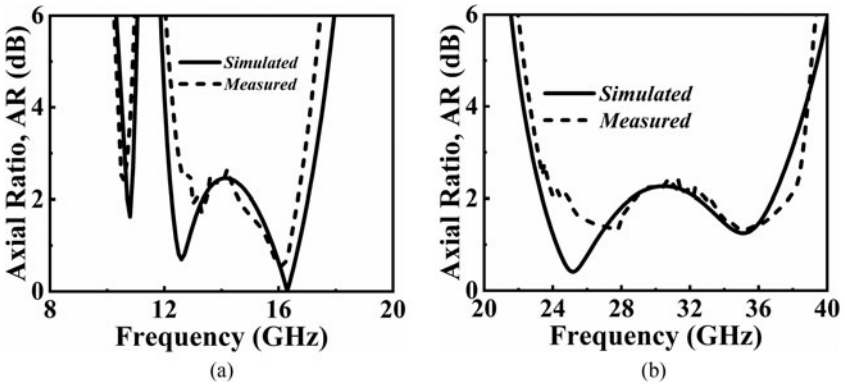

Fig. 16. Comparison of simulated versus measured AR (dB) for (a) X, Ku, and (b) K, Ka-bands.

as the prototype. The receiver antenna is tilted orthogonally by 90° with reference to the transmitter for the cross-pol measurement. For the co-pol measurement, antennas are aligned in the same polarization plane (see Fig. 13(b)), and responses are depicted in Fig. 14. The measured PCR and AR are depicted in Figs 15 and 16, respectively. The performance of the polarizer for different oblique angles under TE and TM modes is investigated. For the TE case, antennas were placed and moved away in steps of 15° from 0° to 45°, such that the incident electric field from the transmitter is always tangential to the metasurface. The antennas were orthogonally oriented for the TM mode of incidences, and the same steps were repeated. The PCR and AR (dB) results for TE and TM are plotted in Figs 17 and 18, respectively. The measured results are in a good agreement with the simulated one. From the authors' knowledge, the proposed design is ultra-compact, with low-profile thickness, showing multi-polarization conversion of both linear–circular (with a different sense of CP), and linear–cross with considerable angular stability. These features make this design suitable for real-time sub-miniaturized applications. It will be clear by comparing the proposed polarizer performance with other recently reported state-of-the-art designs reported in the literature (see Table 3).

Conclusion

This article proposes a multiband linear–circular and linear–cross reflective type polarization converter for different X–Ka band applications. This simple design comprises a meander-line connected to horizontally oriented dipoles on a dielectric substrate. The performance is stable for the oblique incidences in TE and TM cases. Multiple plasmonic resonances are the reason behind

https://doi.org/10.1017/S1759078723000417 Published online by Cambridge University Press

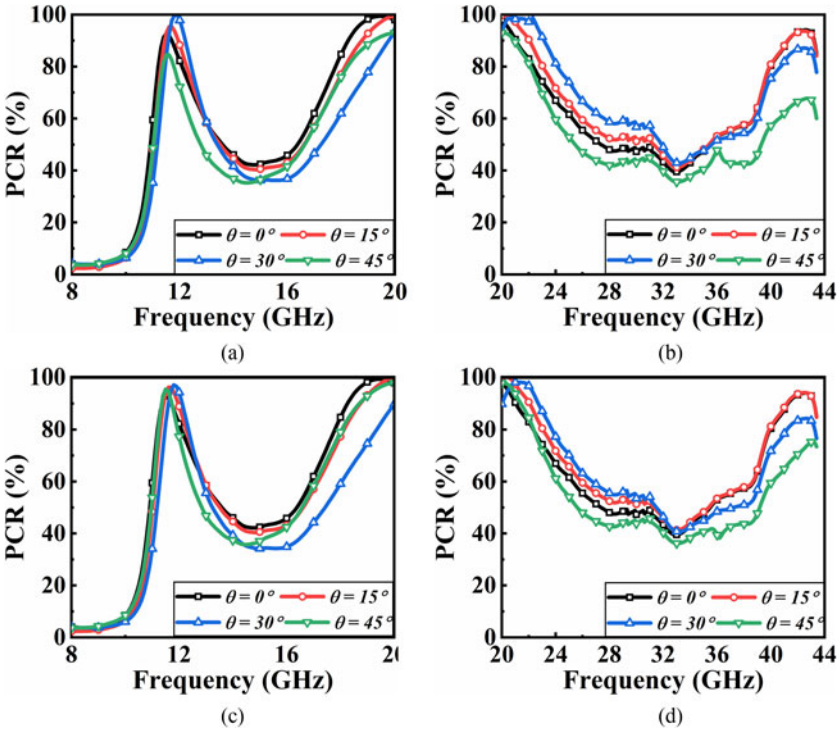

Fig. 17. Comparison of the measured PCR with simulated one under TE for (a) X, Ku, and (b) K, Ka-bands. Under TM incidence of the proposed reflective polarizer for (c) X, Ku, and (d) K, Ka-bands.

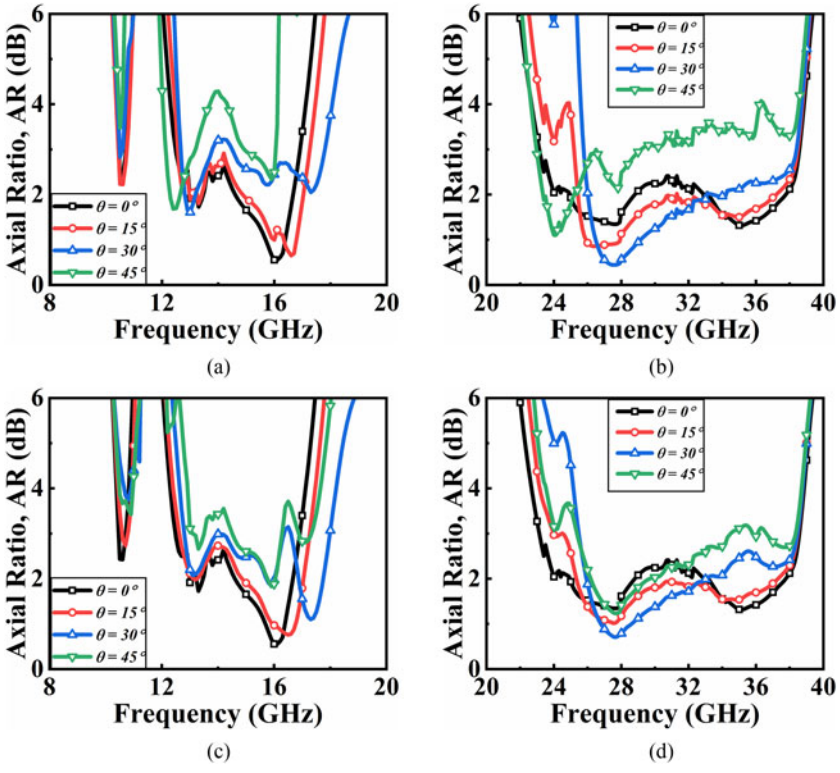

Fig. 18. Comparison of the measured AR (dB) with simulated one under TE for (a) X, Ku, and (b) K, Ka-bands. Under TM incidence of the proposed reflective polarizer for (c) X, Ku, and (d) K, Ka-bands.

the wideband characteristics for different polarization conversions. This structure's novelties lie in the orthogonal circular rotation in consecutive bands, highly miniaturized unitcell architecture possesses more than one polarization conversion in different bands with better angular stability. To the best of the authors' knowledge, these attractive features make the design suitable for satellite communication applications.

Conflict of interest. The authors declare that there are no conflict of interest related to this article.

https://doi.org/10.1017/S1759078723000417 Published online by Cambridge University Press

Table 3. Performance comparison of the proposed design with other recently reported state-of-the-art reflective type polarizers

Ref.	Substrate used	Periodicity (in λ_L^2)	Volume (in λ_L^3/1000)	Polarization conversion	Frequency range (GHz)	FBW (%)	Angular stability	Orthogonality in CP	No. of layers used
[30]	Teflon	0.219 × 0.219	3.932	Linear–cross	8.2–23	94.8	–	–	Single
[14]	Duroid 4730	0.176 × 0.176	1.362	Linear–cross	4.4–5.30	18.56	–	–	Single
					9.45–13.60	36.01			
[31]	FR-4	0.175 × 0.175	1.225	Linear–cross	8–11	31.58	–	–	Single
				Linear–circular	7.5–7.7	2.63			
					11.5–11.9	3.42			
[32]	FR-4	0.091 × 0.091	0.753	Linear–cross	17.4–18.9	8.26	30°	Yes	Dual layered
				Linear–circular	9.1–16.5	57.81			
					20–25.4	23.79			
[33]	F4BM220	0.345 × 0.345	23.269	Linear–circular	6.9–14.1	66.6	–	–	Dual layered
[18]	RT Duroid 5870	0.303 × 0.303	6.280	Linear–circular	20.2–21.2	4.83	Up to 60°	Yes	Dual substrate
					29.5–30.8	4.31			
[8]	Rogers RO3003 and FR-27 Taconic	0.168 × 0.168	3.935	Linear–circular	18–22.2	20.9	Up to 45°	Yes	Dual-layered and dual substrate
					28.7–30.4	5.75			
[21]	PET	0.188 × 0.188	2.820	Linear–cross	11.3–20	56.5	Up to 40°	–	Single
[13]	F4B-2	0.182 × 0.182	2.780	Linear–cross	12.4–27.96	98.9	Up to 40°	–	Single
[10]	Taconic RF-35	0.152 × 0.312	2.820	Linear–circular	11.7–12.5	6.61	Up to 30°	Yes	Single
					17.3–18.1	4.51			
This work	**FR-4**	**0.089 × 0.064**	**0.199**	**Linear–circular**	**10.60–10.92**	**2.97**	**Up to 45°**	**Yes**	**Single**
					12.12–17.32	**35.33**			
					22.72–37.76	**49.74**			
				Linear–cross	**11.41–12**	**5.04**			
					19.01–22.34	**16.11**			
					40.74–46.82	**13.89**			

References

1. **Zhao Y and Alù A** (2011) Manipulating light polarization with ultrathin plasmonic metasurfaces. *Physical Review B: Condensed Matter and Materials Physics* **84**, 205428.
2. **Li J, Guo H, Xu T, Chen L, Hang Z, Zhou L and Chen S (2019) Multiple-beam interference-enabled broadband metamaterial wave plates. *Physical Review Applied* 11, 044042.**
3. **Cheng H, Tian J, Li J, Deng L, Yu P and Chen S** (2013) Mid-infrared tunable optical polarization converter composed of asymmetric graphene nanocrosses. *Optics Letters* **38**, 1567–1569.
4. **Strikwerda AC, Fan K, Tao H, Pilon DV, Zhang X and Averitt RD** (2009) Comparison of birefringent electric split-ring resonator and meanderline structures as quarter-wave plates at terahertz frequencies. *Optics Express* **17**, 136–149.
5. **Shukoor MA and Dey S** (2021) A simple I-shaped wideband linear–linear and linear–circular reflective type polarizer. *2021 IEEE 19th International Symposium on Antenna Technology and Applied Electromagnetics (ANTEM)*, pp. 1–2.
6. **Abdulkarim, Yadgar I, Fatih Özkan Alkurt, Mehmet Bakır, Halgurd N Awl, Fahmi F Muhammadsharif, Muharrem Karaaslan, Bhargav Appasani, Khalid Saeed Lateef Al-Badri, Yuanyuan Zhu and Jian Dong** (2022) A polarization-insensitive triple-band perfect metamaterial absorber incorporating ZnSe for terahertz sensing. *Journal of Optics* **24**, 105102.
7. **Majeed K, Niazi SA, Altintas O, Baqir MA, Karaslaan M and Hasar UC** (2022) Multiband polarization-insensitive cartwheel metamaterial absorber. *Journal of Materials Science* **57**, 21392–21401.
8. **Del Mastro M, Ettorre M and Grbic A** (2020) Dual-band, orthogonally-polarized LP-to-CP converter for SatCom applications. *IEEE Transactions on Antennas and Propagation* **68**, 6764–6776.
9. **Bin Wang H and Cheng YJ** (2019) Single-layer dual-band linear-to-circular polarization converter with wide axial ratio bandwidth and different polarization modes. *IEEE Transactions on Antennas and Propagation* **67**, 4296–4301.
10. **Tang W, Mercader-Pellicer S, Goussetis G, Legay H and Fonseca NJG** (2017) Low-profile compact dual-band unit cell for polarizing surfaces operating in orthogonal polarizations. *IEEE Transactions on Antennas and Propagation* **65**, 1472–1477.
11. **Shukoor MA, Dey S, Koul SK, Poddar AK and Rohde UL** (2021) Broadband linear-cross and circular-circular polarizers with minimal bandwidth reduction at higher oblique angles for RCS applications. *International Journal of RF and Microwave Computer-Aided Engineering* **31,** e22693.
12. **Borgese M, Costa F, Genovesi S, Monorchio A and Manara G** (2018) Optimal design of miniaturized reflecting metasurfaces for ultra-wideband and angularly stable polarization conversion. *Scientific Reports* **8**, 1–11.
13. **Zhao Y, Qi B, Niu T, Mei Z, Qiao L and Zhao Y** (2019) Ultra-wideband and wide-angle polarization rotator based on double W-shaped metasurface. *AIP Advances* **9**, 085013.
14. **Huang X, Yang H, Zhang D and Luo Y** (2019) Ultrathin dual-band metasurface polarization converter. *IEEE Transactions on Antennas and Propagation* **67**, 4636–4641.
15. **Öztürk, Murat, Umur Korkut Sevim, Olcay Altıntaş, Emin Ünal, Oğuzhan Akgöl, Muharrem Karaaslan and Cumali Sabah** (2022) Design of a linear to circular polarization converter integrated into a concrete construction for radome applications. *International Journal of Microwave and Wireless Technologies* **14**, 824–831.
16. **Li Z, Liu W, Cheng H, Chen S and Tian J** (2015) Realizing broadband and invertible linear-to-circular polarization converter with ultrathin single-layer metasurface. *Scientific Reports* **5**, 1–9.
17. **Zeng, Li, Hai-Feng Zhang, Guo-Biao Liu and Tong Huang** (2019) Broadband linear-to-circular polarization conversion realized by the solid state plasma metasurface. *Plasmonics (Norwell, MA)* **14**, 1679–1685.
18. **Arnieri E, Salucci M, Greco F, Boccia L, Massa A and Amendola G** (2022) An equivalent circuit/system by design approach to the design of reflection-type dual-band circular polarizers. *IEEE Transactions on Antennas and Propagation* **70**, 2364–2369.
19. **Lin B, Lv L, Guo J, Liu Z, Ji X and Wu J** (2020) An ultra-wideband reflective linear-to-circular polarization converter based on anisotropic metasurface. *IEEE Access* **8**, 82732–82740.
20. **Zheng Q, Guo C and Ding J** (2018) Wideband metasurface-based reflective polarization converter for linear-to-linear and linear-to-circular polarization conversion. *IEEE Antennas and Wireless Propagation Letters* **17**, 1459–1463.
21. **Wang, Qi, Xiangkun Kong, Xiangxi Yan, Yan Xu, Shaobin Liu, Jinjun Mo and Xiaochun Liu** (2019) Flexible broadband polarization converter based on metasurface at microwave band. *Chinese Physics B* **28**, 074205.
22. **Molero Jimenez C, Menargues E and Garcia-Vigueras M** (2020) All-metal 3-D frequency-selective surface with versatile dual-band polarization conversion. *IEEE Transactions on Antennas and Propagation* **68**, 5431–5441.
23. **Doumanis E, Goussetis G, Gómez-Tornero JL, Cahill R and Fusco V** (2012) Anisotropic impedance surfaces for linear to circular polarization conversion. *IEEE Transactions on Antennas and Propagation* **60**, 212–219.
24. **Chen S, Liu W, Li Z, Cheng H and Tian J** (2017) Polarization state manipulation of electromagnetic waves with metamaterials and Its applications in nanophotonics. *Metamaterials – Devices and Applications*.
25. **Hebib S, Aubert H, Pascal O, Fonseca NJG, Ries L and Lopez JE** (2009) Multiband pyramidal antenna loaded with a cutoff open-ended waveguide. *IEEE Transactions on Antennas and Propagation* **57**, 266–270.
26. **Naseri P, Matos SA, Costa JR, Fernandes CA and Fonseca NJG** (2018) Dual-band dual-linear-to-circular polarization converter in transmission mode application to band satellite communications. *IEEE Transactions on Antennas and Propagation* **66**, 7128–7137.
27. **Shukoor MA, Dey S and Koul SK** (2022) Broadband chiral-type linear to linear reflecting polarizer with minimal bandwidth reduction at higher oblique angles for satellite applications. *IEEE Transactions on Antennas and Propagation* **70**, 5614–5622.
28. **Bin Wang H, Cheng YJ and Chen ZN** (2020) Wideband and wide-angle single-layered-substrate linear-to-circular polarization metasurface converter. *IEEE Transactions on Antennas and Propagation* **68**, 1186–1191.
29. **Luukkonen, Olli, Constantin Simovski, Gérard Granet, George Goussetis, Dmitri Lioubtchenko, Antti V Raisanen and Sergei A Tretyakov** (2008) Simple and accurate analytical model of planar grids and high-impedance surfaces comprising metal strips or patches. *IEEE Transactions on Antennas and Propagation* **56**, 1624–1632.
30. **Li, Fengxia, Haiyan Chen, Linbo Zhang, Yang Zhou, Jianliang Xie, Longjiang Deng and Vincent G Harris** (2019) Compact high-efficiency broadband metamaterial polarizing reflector at microwave frequencies. *IEEE Transactions on Microwave Theory and Techniques* **67**, 606–614.
31. **Khan MI, Khalid Z and Tahir FA** (2019) Linear and circular-polarization conversion in X-band using anisotropic metasurface. *Scientific Reports* **9**, 1–11.
32. **Liu, Xiaobo, Jingsi Zhang, Wei Li, Rui Lu, Lumei Li, Zhuo Xu and Anxue Zhang** (2017) Three-band polarization converter based on reflective metasurface. *IEEE Antennas and Wireless Propagation Letters* **16**, 924–927.
33. **Ibrahim MS, Mahmoud A, Awamry A, Jiang ZH, Hong W and Al-Nuaimi M** (2019) Design and fabrication of engineered reflector for wideband linear-to-circular polarization converter. *2019 IEEE International Symposium on Antennas and Propagation and USNC-URSI Radio Science Meeting, APSURSI 2019 – Proceedings*, pp. 1697–1698.

Mohammad Abdul Shukoor (graduate student member, IEEE) earned his bachelor's degree (B.Tech.) from Electronics and Communication Engineering Department from RVR & JC College of Engineering, Guntur, India, in 2013, his master's degree (M.Tech.) in radar and microwave engineering from Andhra University, Visakhapatnam, India, in 2016. He is working toward a Ph.D. with the Department of Electrical Engineering, Indian Institute of Technology Palakkad, Kerala, India. His current research interests include metamaterial-based absorbers, FSSs, and polarization converters. He has published more than 33 research articles and has filed four Indian patents. Now, Shukoor is working as a post-doctoral fellow at Wireless Communications Lab, Department of Electronics and Communication, Indian Institute of Technology Roorkee, Roorkee, India. Shukoor was the recipient of the Best Paper Awards in IEEE Conferences like

https://doi.org/10.1017/S1759078723000417 Published online by Cambridge University Press

International IoT Electronics and Mechatronics Conference, Vancouver, BC, Canada, in 2020, and WAMS 2022.

Sukomal Dey (senior member, IEEE) earned his B.Tech. in electronics and communication engineering from the West Bengal University of Technology, Kolkata, India, in 2006, his M.Tech. in mechatronics engineering from the Indian Institute of Engineering Science and Technology, Shibpur, India, in 2008, and his Ph.D. from the Centre for Applied Research in Electronics, Indian Institute of Technology Delhi, New Delhi, India, in July 2015. From August 2015 to July 2016, he was a project scientist with Industrial Research and Development Centre, IIT Delhi, and also worked on a collaborative research project supported by Synergy Microwave Corp., Paterson, NJ, USA. From August 2016 to June 2018, he was with Radio Frequency Microsystem Lab, National Tsing Hua University, Taiwan, as a postdoctorate research fellow. Since June 2018, he has been an assistant professor with the Department of Electrical Engineering, Indian Institute of Technology Palakkad, Palakkad, India. During his M.Tech. (1 year), he was with Central Electronics Engineering Research Institute, Pilani, India, in 2009. He has authored or coauthored more than 120 research papers, two state-of-the-art books, two book chapters, and has filed 17 patents. His research interests include electromagnetic metamaterial structures, frequency selective surfaces, microwave imaging, and microwave-integrated circuits, including antennas and RFMEMS. Dr. Dey was the recipient of the Postgraduate Student Award from the Institute of Smart Structure and System, Bangalore, India, in 2012, Best Industry Relevant Ph.D. Thesis Award from the Foundation for Innovation in Technology Transfer, IIT Delhi, in 2016, Distinction in Doctoral Research – 2016 from IIT Delhi, Postdoctoral Fellow Scholarships from the Ministry of Science and Technology, Taiwan, in 2016 and 2017, respectively, Early Career Research Award from the Science and Engineering Research Board (SERB), Government of India, in 2019, Smt. Ranjana Pal Memorial Award (2021) from the Institution of Electronics and Communication Engineers, and several best paper awards from national and international IEEE conferences with his students. He has been inducted in the technical program committee 4 and 6 of the IEEE MTT Society.

https://doi.org/10.1017/S1759078723000417 Published online by Cambridge University Press